

Effect of Quantum and Dielectric Confinement on the Exciton–Exciton Interaction Energy in Type II Core/Shell Semiconductor Nanocrystals

Andrei Piryatinski,^{*,†} Sergei A. Ivanov,^{‡,§} Sergei Tretiak,^{†,§} and Victor I. Klimov^{*,‡,§}

Center for Nonlinear Studies (CNLS), Theoretical Division, C-PCS, Chemistry Division, and Center for Integrated Nanotechnologies (CINT), Los Alamos National Laboratory, Los Alamos, New Mexico 87545

Received September 22, 2006; Revised Manuscript Received November 3, 2006

ABSTRACT

We study theoretically two electron–hole pair states (biexcitons) in core/shell hetero-nanocrystals with type II alignment of energy states, which promotes spatial separation of electrons and holes. To describe Coulomb interactions in these structures, we apply first-order perturbation theory, in which we use an explicit form of the Coulomb-coupling operator that takes into account interface-polarization effects. This formalism is used to analyze the exciton–exciton interaction energy as a function of the core and shell sizes and their dielectric properties. Our analysis shows that the combined contributions from quantum and dielectric confinement can result in strong exciton–exciton repulsion with giant interaction energies on the order of 100 meV. Potential applications of strongly interacting biexciton states include such areas as lasing, nonlinear optics, and quantum information.

Introduction. The use of semiconductor hetero-nanostructures opens interesting opportunities for controlling materials' properties via direct manipulation of electronic wavefunctions. This concept of "wavefunction engineering" has been extensively explored in the case of epitaxial quantum wells and superlattices. Heterostructuring is also becoming more common in the field of chemically synthesized semiconductor nanocrystals (NCs) or nanocrystal quantum dots. One typical approach in this case is the use of a wide-gap semiconductor for overcoating a core made of a narrower-gap material, which allows one to significantly improve emission quantum yields by reducing surface-related nonradiative carrier losses.^{1–7} In such NCs, both an electron and a hole reside in the same part of the heterostructure (the NC core), which corresponds to the type I localization regime.

There are also several recent examples of type II core/shell NCs, in which the alignment of energy states at the interface between two semiconductors promotes spatial separation of electrons and holes between the core and the shell.^{8–11} The type II regime provides new means for tuning both spectral and dynamical responses of NCs. Specifically, in this case one can control radiative decay by tuning the overlap between the electron and hole wavefunctions.⁹

Further, type II NCs can be engineered to emit at energies that are lower than the band gap of either semiconductor comprising a heterostructure, which is a useful capability for the development of, e.g., new infrared-emitting chromophores.⁸

Type II structures also provide interesting opportunities for tuning carrier–carrier interactions in NCs, which is an important capability for such applications as lasing,^{10,12} nonlinear optics,^{13,14} and photodetectors and photovoltaic cells utilizing carrier multiplication.^{15,16} For example, a serious complication for lasing applications of NCs arises from nonradiative multiparticle Auger recombination, which leads to short, picosecond lifetimes of optical gain.^{12,17} Recently we experimentally demonstrated that using ZnSe-(core)/CdSe(shell) NCs tunable between type I and type II localization regimes we could control Auger recombination rates.¹⁸ Specifically, we observed suppression of Auger decay in the case of shell localization of electrons, which resulted in decreased Coulomb coupling between photoexcited carriers.

Another strategy for improving the lasing performance of NCs involves realization of strong exciton–exciton (X–X) repulsion, which can be utilized for displacing an "absorbing" transition in singly excited NCs with respect to the emission line.¹⁰ This approach can potentially allow lasing in the single-exciton regime, for which Auger recombination is

* Corresponding authors. E-mail: apiryat@lanl.gov; klimov@lanl.gov.

[†] Center for Nonlinear Studies, Theoretical Division.

[‡] C-PCS, Chemistry Division.

[§] Center for Integrated Nanotechnologies.

simply inactive. This concept, however, cannot be realized using traditional type I NCs, in which the X–X interaction is attractive (as shown, e.g., experimentally¹⁹) and hence the interaction energy (Δ_{XX}) is negative. On the other hand, by separating electrons and holes spatially, one can increase the repulsive component of the interaction energy, which can reverse the sign of Δ_{XX} as was previously demonstrated for type II double quantum-well structures.²⁰ In the case of strongly confined type II NCs, this strategy can lead not only to overall X–X repulsion but also to large magnitudes of interaction energies, which can be produced because of very small separation between interacting charges. Large values of Δ_{XX} are important for practical realization of the concept of single-exciton lasing, because in order to eliminate interference from the “absorbing” transition its Coulomb shift (determined by Δ_{XX}) should be comparable to or greater than the transition line width. The latter is on the order of 100 meV even in the best highly monodisperse NC samples.

Previous theoretical studies of X–X interactions in strongly confined quantum dots have focused exclusively on type I nanostructures.^{21–26} One significant complication in this case is the difficulty in applying standard perturbation approaches. Specifically, because of almost identical spatial distributions of electron and hole wavefunctions that are obtained in the single-electron- and single-hole-band model (referred below as the two-band model), the effective charge density associated with a single exciton state is nearly zero, which leads to a nearly zero value of the first-order contribution to the X–X interaction energy. Therefore, perturbative treatment in this case requires the use of more complex computational schemes that account for higher-order perturbation terms.

One approach to overcome this problem is the use of a variational ansatz.²³ However, for small-radius dots it predicts positive values of the X–X interaction energy (i.e., effective X–X repulsion) for both single and multiple hole bands.^{23,25,26} On the other hand, an asymptotic analysis using second-order perturbation theory²² as well as experimental results¹⁹ show that even for small quantum dots Δ_{XX} is negative, which corresponds to X–X attraction. Because of these complications, theoretical treatment of X–X interactions in type I strongly confined NCs still represents a significant challenge. Paradoxically, this problem is less challenging in the case of type II NCs despite their more complex multicomponent structure. In this case, spatial separation of electrons and holes significantly distorts charge quasi-neutrality existing in type I systems and allows one to accurately evaluate X–X interaction energies within first-order perturbation theory.

In this Letter, we analyze theoretically X–X interactions in type II core/shell NCs within the two-band model and using first-order perturbation theory to account for both quantum and dielectric confinement. The latter effect is due to discontinuity of the dielectric constant at the core–shell interface, and we treat it within the image-charge approach. Our modeling indicates that in type II hetero-NCs the X–X interaction is indeed repulsive and can be characterized by giant interaction energies up to ca. 100 meV. Large magnitudes of Δ_{XX} that are comparable to typical transition

line widths of NC samples indicate the feasibility of single-exciton NC lasing using X–X repulsion.

Description of the Model. In this work, we study small-size semiconductor NCs, for which carrier confinement (kinetic) energies are much greater than Coulomb interaction energies, which hence can be treated using perturbation approaches.^{25–27} In our calculations, we first evaluate wavefunctions of an electron and a hole without taking into account Coulomb effects. Then, we calculate the Coulomb correction to the energy of a single electron–hole pair state (single-exciton state) using the first-order perturbation term, which accounts for the electron–hole interaction. Finally, we compute the X–X interaction energy by applying first-order perturbation theory to the lowest-energy biexciton, which comprises two ground-state electrons and two ground-state holes. In our calculations of both single- and biexciton energies, we explicitly account for dielectric-confinement effects interpreted using the image-charge approach.

To describe quantum states in a spherically symmetric type II core/shell NC (Figure 1) characterized by the core radius R and the shell width H , we use the effective mass approximation. We assume the existence of single energy bands for both electrons and holes. This assumption represents a simplification compared to multiband models that explicitly take into account mixing between, e.g., different valence sub-bands.²⁷ However, this simplified approach still allows us to capture the essential trends of core- and shell-size dependences of exciton and biexciton energies. To find electron and hole eigenstates and eigenvalues, we solve the envelope-function Schrödinger equation using a spherically symmetric confinement potential energy operator, which only depends on the radial coordinate r .^{27,28} In our calculations, we consider type II core/shell NCs of two different geometries illustrated in parts A and B of Figure 1. One geometry (Figure 1A, referred to below as the e/h structure) corresponds to the situation for which an electron is localized in the core while a hole is in the shell. In the other geometry (Figure 1B, the h/e structure), the electron and the hole switch the regions of their localization. For the e/h structure, the electron ($\hat{U}^e(r)$) and the hole ($\hat{U}^h(r)$) confinement operators can be presented as follows (Figure 1A): $\hat{U}^e(r) = 0$ for $0 \leq r < R$, $\hat{U}^e(r) = U_0^e$ for $R \leq r < R + H$, and $\hat{U}^e(r) = \infty$ for $r \geq R + H$; $\hat{U}^h(r) = U_0^h$ for $0 \leq r < R$, $\hat{U}^h(r) = 0$ for $R \leq r < R + H$, and $\hat{U}^h(r) = \infty$ for $r \geq R + H$. Corresponding operators for the h/e structures have the following form (Figure 1B): $\hat{U}^e(r) = U_0^e$ for $0 \leq r < R$, $\hat{U}^e(r) = 0$ for $R \leq r < R + H$, and $\hat{U}^e(r) = \infty$ for $r \geq R + H$; $\hat{U}^h(r) = 0$ for $0 \leq r < R$, $\hat{U}^h(r) = U_0^h$ for $R \leq r < R + H$, and $\hat{U}^h(r) = \infty$ for $r \geq R + H$. Both structures exhibit a “spatially indirect” energy gap (E_g), which is determined by the separation between the bottom of the conduction band of one semiconductor comprising a hetero-NC and the top of the valence bands of the other semiconductor.

First, we find solutions of the envelope-function Schrödinger equation for noninteracting electrons and holes using boundary conditions according to which the radial wavefunction is finite at the center of the core and is zero outside the shell. An additional boundary condition is imposed by

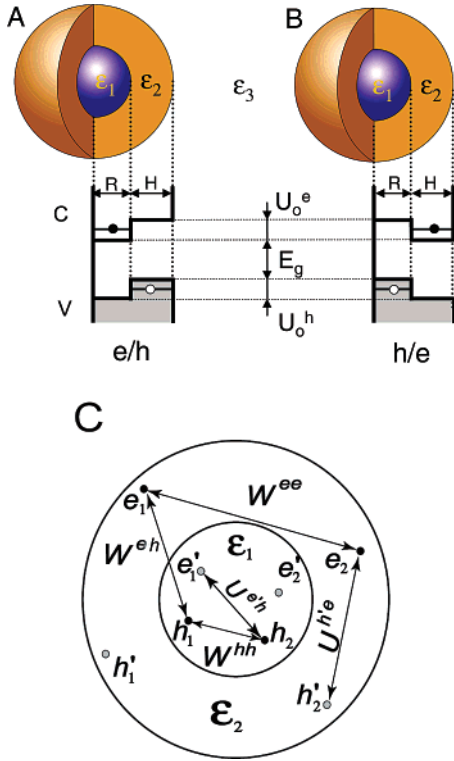


Figure 1. Schematics of type II core/shell NCs along with typical profiles of the valance (labeled V) and conduction (labeled C) band confinement potentials. (A) The e/h nanostructure in which an electron is localized in the core and a hole in the shell. (B) The h/e nanostructure, in which the electron and the hole switch regions of localization. (C) Biexciton state in h/e nanostructure comprising two electrons, e_1 and e_2 , and two holes, h_1 and h_2 . The core–shell interface polarization can be described in terms of additional fields generated by the images of these four charges labeled as e_1' , e_2' , h_1' , and h_2' . Arrows show different components of the Coulomb interaction between the carriers that contribute to the X–X interaction energy (see text for details).

the requirement of continuity of the current at the core–shell interface, which translates into the requirements for continuity of both the radial wavefunctions and their effective-mass-weighted derivatives at the heterointerface.²⁸ In our calculations, we only consider the lowest-energy, zero-angular-momentum, conduction- and valence-band 1S states. The solution of the Schrödinger equation that satisfies the above boundary conditions is

$$\mathcal{R}^a(r) = N^a \frac{\sin(k^a r)}{r \sin(k^a R)} \quad \text{for } 0 \leq r < R \quad (1)$$

$$\mathcal{R}^a(r) = N^a \frac{\sin(q^a(R + H - r))}{r \sin(q^a H)} \quad \text{for } R \leq r < R + H$$

where $a = e, h$ for electrons and holes, respectively, and N^a is the normalization constant derived from the condition that the integral of $\mathcal{R}^a(r)$ over the hetero-NC volume is unity. In the case of the e/h nanostructure, the electron wavevector components are $k^e = (2m_c^e E^e / \hbar^2)^{1/2}$ and $q^e = (2m_s^e (E^e - U_0^e) / \hbar^2)^{1/2}$, whereas the hole wavevector components are $k^h = (2m_c^h (E^h - U_0^h) / \hbar^2)^{1/2}$ and $q^h = (2m_s^h E^h / \hbar^2)^{1/2}$, where m_c^a

and m_s^a ($a = e, h$) are carrier effective masses for the core (index c) and the shell (index s), and E^a is the electron ($a = e$) or hole ($a = h$) energy. For h/e nanostructures, the electron and hole wavevectors can be obtained by switching the e and h superscripts in the above expressions. The 1S eigenenergy E^a , can be obtained as the lowest root of the following equation³⁰

$$[1 - k^a R \cot(k^a R)] m_s^a / m_c^a = 1 + q^a R \cot(q^a H) \quad (2)$$

In our modeling we use an energy criterion for defining the boundaries between various localization regimes. Specifically, in the case of the e/h structures (Figure 1A), we assume that an electron is primarily localized in the core if its lowest-energy level is located below the conduction band offset at the interface given by U_0^e . On the other hand, a hole is shell-localized if $E^h < U_0^h$. Similar conditions can be obtained for the h/e structure (Figure 1B) to define regimes that correspond to shell localization of electrons and core localization of holes. Using the above considerations, we can obtain the following equation for determining the minimum core radius R_{cl} for which the electron (hole) becomes *core-localized* in the e/h (h/e) structure for a given shell width H

$$H = - \frac{m_c^a / m_s^a R_{cl}}{1 - m_c^a / m_s^a + k_1^a R_{cl} \cot(k_1^a R_{cl})}, \quad a = e, h \quad (3)$$

Here $k_1^a = (2m_c^a U_0^a)^{1/2} / \hbar$ and $x_1 < k_1^a R_{cl} < \pi$, where x_1 is the first root of the equation $x \cot(x) + m_s^a / m_c^a = 1$. According to eq 3, the 1S level is below the shell step potential U_0^a for $R > R_{cl}(H)$. Similarly, the minimum value of the shell width, H_{sl} , which results in *shell localization* of the 1S state for a given radius R can be derived from the following equation

$$R = -\tan(q_1^a H_{sl}) q_1^a, \quad a = e, h \quad (4)$$

where $q_1^a = (2m_s^a U_0^a)^{1/2} / \hbar$ and $\pi/2 < q_1^a H_{sl} < \pi$. The condition $H > H_{sl}(R)$ corresponds to shell localization of holes ($a = h$) in e/h structures or shell localization of electrons ($a = e$) in h/e structures.

As a quantitative measure of the spatial separation between electrons and holes in a hetero-NC, we use an overlap integral between electron and hole wavefunctions defined as

$$\Theta = \left| \int_0^{R+H} dr r^2 \mathcal{R}^e(r) \mathcal{R}^h(r) \right|^2 \quad (5)$$

This quantity also relates to imbalance between negative and positive charges in the NC, and as shown below, the changes in Θ directly correlate with changes in Δ_{XX} . Another meaning of the overlap integral is that it determines the strength of the interband 1S–1S optical transition.

On the basis of the conditions given by eqs 3 and 4, we can map the regions of (R, H) -space that correspond to different localization regimes, which results in the localiza-

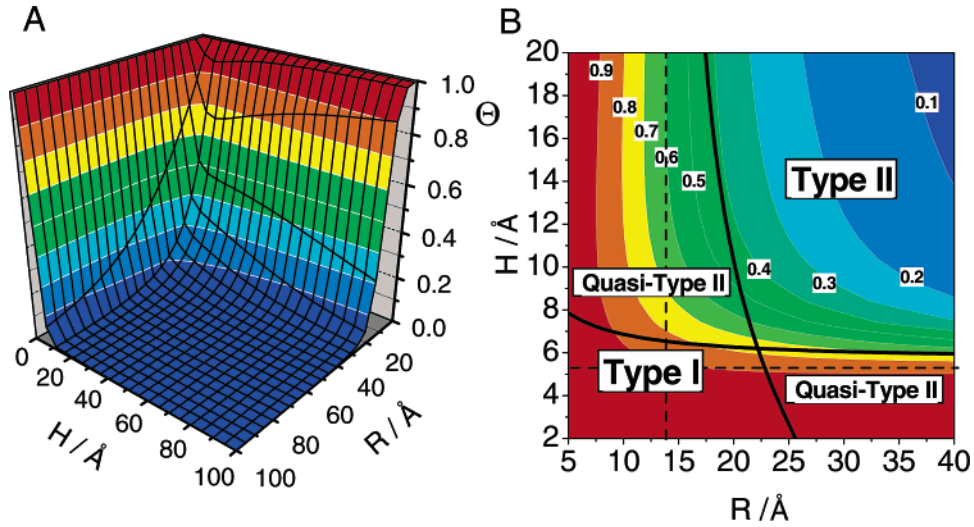


Figure 2. (A) A three-dimensional plot of the overlap integral Θ (eq 5) as a function of the core radius R and shell width H in the e/h structure. (B) A reduced-scale contour plot of the electron–hole overlap integral and the localization phase diagram that shows the regions of (R, H) -space that correspond to different localization regimes in e/h hetero-NCs. The black solid line, which goes from top to bottom, represents the boundary between regimes for which the electron either is delocalized over the entire hetero-NC volume (left of the line) or is core-localized (right of the line). This line is derived from eq 3 for R_{cl} . The dashed vertical line is the asymptotic, large- H limit of R_{cl} . The black solid line, which goes from left to right, separates the regimes for which the hole either is delocalized over the entire hetero-NC volume (below the line) or is shell localized (above the line). This line is derived from eq 4 for H_{sl} . The dashed horizontal line is the asymptotic, large- R limit of H_{sl} .

tion phase diagram displayed in Figure 2B. To illustrate the effect of changes in carrier localization on the electron–hole overlap integral, in the same figure we also indicate the Θ values as a function of H and R . In the type I regime, which occurs for $R < R_{cl}$ and $H < H_{cl}$, both an electron and a hole are delocalized over the entire hetero-NC volume. In the type II regime ($R > R_{cl}$ and $H > H_{cl}$), electrons and holes are localized in the core and the shell, respectively. In addition to regions with well-defined type I and type II regimes, the localization phase diagram also shows two areas that correspond to partial separation between electron and hole wavefunctions. This regime (labeled in Figure 2B as quasi-type II) occurs for $R > R_{cl}$ and $H < H_{cl}$ (the electron is core-localized but the hole is delocalized over the entire NC) or $R < R_{cl}$ and $H > H_{cl}$ (the hole is shell-localized but the electron is delocalized over the entire NC).

Next, we calculate the leading contribution to the Coulomb corrections to the single-exciton energy. In a heterostructure with dielectric interfaces the carrier–carrier interaction operator has two components (see the diagram in Figure 1C, which illustrates the different types of Coulomb interaction terms in a core/shell NC). One of them is due to direct Coulomb coupling screened by a dielectric medium, and it can be represented as

$$W^{ab} = \int_0^{R+H} dr_a r_a^2 \int_0^{R+H} dr_b r_b^2 \rho^a(r_a) \hat{W}(r_a, r_b) \rho^b(r_b) \quad (6)$$

The other component is due to the interface polarization energy, which we describe by interactions between charges and their images excluding the interaction between a charge and its own image

$$U^{ab} = \int_0^{R+H} dr_a r_a^2 \int_0^{R+H} dr_b r_b^2 \rho^a(r_a) \hat{U}(r_a, r_b) \rho^b(r_b) \quad (7)$$

In the above expressions, $\rho^a(r_a) = |\mathcal{R}^a(r)|^2$ is the electron or hole density and $a, b = e, h$ or h, e ; $\hat{W}(r_a, r_b)$ is the spherically symmetric component of the point charges direct Coulomb interaction operator, and $\hat{U}(r_a, r_b)$ is the same component of the polarization energy operator. To obtain the explicit form of these operators, we solve analytically the Poisson equation for a potential due to a point charge in the core/shell structure with the standard boundary conditions that account for discontinuity of the dielectric constant at heterointerfaces.²⁹ As a result, we obtain the following solutions

$$\hat{W}(r_a, r_b) = \theta(R - r_a)\theta(R - r_b) \frac{q_a q_b}{\epsilon_1 r_>} + [\theta(r_a - R) + \theta(r_b - R)] \frac{q_a q_b}{2\epsilon_2 r_>} \quad (8)$$

$$\hat{U}(r_a, r_b) = \theta(R - r_a)\theta(R - r_b) \frac{q_a q_b (\epsilon_1/\epsilon_2 - 1)}{\epsilon_1 R} + \frac{q_a q_b (\epsilon_2/\epsilon_3 - 1)}{\epsilon_2 (R + H)} \quad (9)$$

where $r_> \equiv \max(r_a, r_b)$; $0 \leq (r_a, r_b) < R + H$; ϵ_1, ϵ_2 , and ϵ_3 are the dielectric constants of the core, the shell, and the environment, respectively; and $\theta(x)$ is the Heaviside step function.

The remaining contribution to the net Coulomb energy (not shown in Figure 1C) comes from the self-interaction of each charge with its own image, which is the so-called dielectric solvation energy (V^a , $a = e, h$). As we demonstrate below, this quantity does not affect the X–X interaction energy; therefore, we do not provide an explicit expression

for it. Taking into account all relevant Coulomb terms, we can write the following expression for the energy of the 1S single-exciton state that comprises the 1S electron and the 1S hole

$$E_X = E_g + E^e + E^h + W^{eh} + U^{eh} + V^e + V^h \quad (10)$$

Next, we consider the lowest-energy biexciton state, which is composed of two 1S excitons. It is natural to describe it in terms of a product of wavefunctions of two 1S electrons and two 1S holes: $\Psi_{XX}(r_{e1}, r_{e2}, r_{h1}, r_{h2}) = \mathcal{R}^e(r_{e1})\mathcal{R}^e(r_{e2}) \times \mathcal{R}^h(r_{h1})\mathcal{R}^h(r_{h2})$. Further, using first-order perturbation theory we can obtain the following expression for the total biexciton energy

$$E_{XX} = 2E_g + 2E^e + 2E^h + W^{ee} + U^{ee} + 4(W^{eh} + U^{eh}) + W^{hh} + U^{hh} + 2V^e + 2V^h \quad (11)$$

Here, the first three terms on the right are due to the bulk energy gap and carrier confinement (kinetic) energies. The rest of the terms are due to the Coulomb interactions described by eqs 6–9 and the carrier dielectric-solvation energies. In this case, eqs 7 and 8 are used to calculate both the electron–hole interaction energies (W^{eh} and U^{eh}) and the energies of interaction between charges of the same sign (W^{aa} and U^{aa} , where $a = e, h$).

Using eqs 10 and 11, we can calculate the X–X interaction energy as $\Delta_{XX} = E_{XX} - 2E_X$. Note that the X–X interaction energy Δ_{XX} defined in this way has the same amplitude but the opposite sign compared to the *biexciton binding energy*, which is often introduced in studies of X–X interactions. This expression indicates that the confinement and the dielectric solvation energy terms that enter E_{XX} are canceled by identical terms in $2E_X$. The surviving contribution to Δ_{XX} is

$$\Delta_{XX} = W_{XX} + U_{XX} \quad (12)$$

The first term on the right is direct Coulomb coupling, which can be represented as

$$W_{XX} = \int_0^{R+H} dr_1 r_1^2 \int_0^{R+H} dr_2 r_2^2 [\rho^e(r_1) - \rho^h(r_1)] \times \hat{W}(r_1, r_2) [\rho^e(r_2) - \rho^h(r_2)] \quad (13)$$

This term depends on the local differences between the electron and hole densities (local charge imbalance) and on the Coulomb operator $\hat{W}(r_1, r_2)$ (eq 8), in which we set $q_a = q_b = q_e$ (bare electron charge). The second contribution to Δ_{XX} comes from the core–shell interface polarization, which is given by

$$U_{XX} = \left(\frac{1}{\epsilon_2} - \frac{1}{\epsilon_1} \right) \frac{q_e^2}{R} (P_c^e - P_c^h)^2 \quad (14)$$

Here, $P_c^a = \int_0^R dr_a r_a^2 \rho^a(r_a)$ denotes the probabilities of finding an electron ($a = e$) or a hole ($a = h$) in the core.

Within the two-band model considered here, there is no spatial separation between the electron and the hole charge densities in type I NCs. In this case, the first-order contribution to Δ_{XX} vanishes; therefore, calculations of the X–X interaction energy require the use of higher-order perturbation terms. The situation is, however, different in type II core/shell NCs, in which electrons and holes are spatially separated and, hence, the local charge density is nonzero. In this case, first-order perturbation theory can be applied to accurately evaluate Δ_{XX} .

Numerical Results and Discussion. Equations 12–14 indicate that in a core/shell NC, the X–X interaction energy depends on both the spatial distribution of charges within the nanostructure and dielectric properties of the core and the shell. To study the main trends in the dependence of Δ_{XX} on the geometrical and dielectric parameters of the NC, we perform numerical simulations using eqs 12–14 for calculating interaction energies and eqs 1 and 2 for calculating eigenstates and eigenenergies. We further use the criteria given by eqs 3 and 4 for distinguishing between different localization regimes. The overlap integral given by eq 5 is used for quantifying the degree of spatial separation between electron and hole wavefunctions.

In our numerical modeling, we use material parameters that are close to those of “real” semiconductors (e.g., ZnSe, ZnTe, CdSe, and CdS). The core radius R and the shell width H are varied between 2 and 100 Å. In both e/h and h/e nanostructure cases, the energy offset at the heterointerface (U_0^e and U_0^h) is assumed to be identical for both the conduction and the valence band and is set to 0.5 eV. The electron and hole effective masses used in these calculations are $0.1m_e$ and $0.6m_e$ (m_e is the free electron mass), respectively, and they are assumed to be the same for the core and the shell. The core (ϵ_1) and shell (ϵ_2) dielectric constants are varied in the range between 4 and 8. Within the adopted formalism, the X–X interaction energy does not depend on the band gap E_g and the dielectric constant of the surrounding medium (ϵ_3).

We first consider the e/h geometry (Figure 1A). To examine the effect of the geometrical parameters on the electron–hole overlap integral and the X–X interaction energy, we fix the dielectric constants ($\epsilon_1 = 4.0$ and $\epsilon_2 = 6.0$) and vary the core radius and the shell thickness. Figure 2A shows Θ as a function of R and H . The general trend is that the increase in R for a fixed H leads to a rapid decrease of Θ indicating a progressive increase in separation of electron and hole wavefunctions. Comparison of the overlap integral and the phase diagram for type I and II localization regimes in Figure 2B indicates that for core radii $R \gtrsim 20$ Å, one can reach a true type II regime with a relatively thin shell ($H_{sl} \approx 6$ Å). For example, with $R = 25$ Å, one can obtain $\Theta < 0.5$ using a shell with $H \gtrsim 8$ Å. This is important from the practical perspective because fabrication of core/shell NCs with thinner shells is less challenging synthetically.

Figure 3A shows the R and H dependence of the W_{XX} component of the X–X interaction energy, which is due to direct Coulomb coupling between charges (eqs 8 and 13). For small radii and small shell thicknesses ($R, H \lesssim 10$ Å),

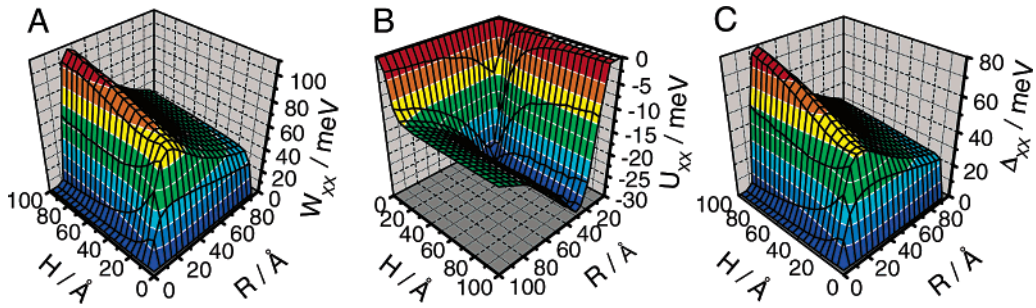


Figure 3. A three-dimensional plot of dependencies on the core radius R and shell width H for (A) the direct Coulomb coupling W_{XX} (eq 13), (B) the core–shell interface polarization energy U_{XX} (eq 14), and (C) the biexciton interaction energy Δ_{XX} (eq 12) (calculated for $\epsilon_1 = 4.0$ and $\epsilon_2 = 6.0$).

$\Theta \approx 1$ (type I localization). In this case, W_{XX} is nearly zero as expected for our approach, which does not account for higher-order perturbation terms. In the range of larger R and H (≥ 10 Å), for which Θ decreases, W_{XX} rapidly increases and ultimately reaches values that are as large as 100 meV. Further, we observe that the sign of W_{XX} is always positive, which indicates that spatial separation between negative and positive charges during the transition to the type II regime leads to the development of strong X–X repulsion which dominates over attractive interactions.

The contribution to Δ_{XX} associated with the core–shell interface polarization U_{XX} is shown in Figure 3B. According to eq 14, its sign solely depends on the sign of the dielectric constant prefactor ($\epsilon_2^{-1} - \epsilon_1^{-1}$) and is negative (attractive interaction) if $\epsilon_2 > \epsilon_1$, which corresponds to the situation considered here. The scaling of U_{XX} with respect to R and H is determined by the interplay between the $1/R$ multiplier and the charge-imbalance factor $(P_c^e - P_c^h)^2$. In the range of $R, H \lesssim 10$ Å (type I localization), where the overlap integral $\Theta \approx 1$ (Figure 3A,B), the polarization contribution vanishes because of a nearly zero charge-imbalance factor. In the region of $10 \lesssim (R, H) \lesssim 20$ Å (transition from type I to II localization) where Θ becomes smaller than unity and, consequently $(P_c^e - P_c^h)^2$, significantly deviates from zero, the polarization term depends on both R and H . Finally, for $R, H \gtrsim 30$ Å (type II localization) where $\Theta \approx 0$ and the charge-imbalance factor approaches its maximum value of 1, U_{XX} becomes independent of H and scales as $1/R$. In this region, the magnitude of the polarization contribution reaches its maximum value of ~ 30 meV.

The total interaction energy, Δ_{XX} (Figure 3C), is a sum of W_{XX} and U_{XX} (eq 12) and is mainly determined by a positive contribution from W_{XX} while U_{XX} provides a relatively small negative correction which does not exceed 20–30% of W_{XX} . As indicated by our numerical modeling the dependence of Δ_{XX} on R and H is qualitatively similar to that in Figure 3C for the whole range of dielectric constants from 4 to 8 studied here. In the case of $\epsilon_1 = \epsilon_2$ the contribution from interface polarization is zero ($U_{XX} = 0$). For $\epsilon_1 > \epsilon_2$, U_{XX} changes sign but is still only 20–30% of the total value of Δ_{XX} . For the entire parameter space investigated here, the sign of Δ_{XX} is positive indicating that excitons tend to repel each other in the core/shell nanostructures studied in this work.

To gain a better understanding of the effect of the spatial distribution of charges and dielectric confinement on Δ_{XX} ,

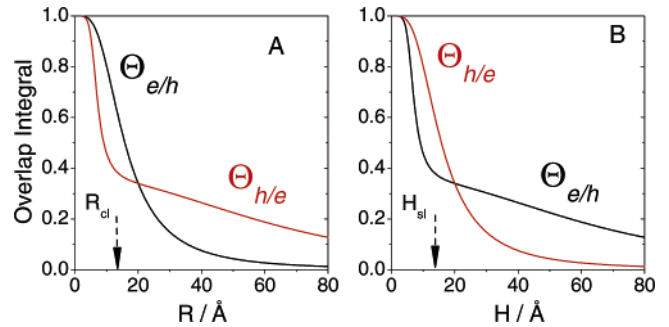


Figure 4. The overlap integral (eq 5) $\Theta_{e/h}$ ($\Theta_{h/e}$) for the e/h (h/e) nanostructure, as (A) a function of core radius R for a fixed shell width ($H = 20$ Å) and (B) a function of H for a fixed core radius ($R = 20$ Å). The point of intersection of $\Theta_{e/h}$ and $\Theta_{h/e}$ approximately corresponds to R_{cl} (panel A) and H_{sl} (panel B) calculated for electrons.

we analyze slices of the dependencies $\Theta = \Theta(R, H)$ (Figure 4) and $\Delta_{XX} = \Delta_{XX}(R, H)$ (Figure 5) by fixing either H or R . We perform calculations for both the e/h and the h/e nanostructures with ϵ_1 and ϵ_2 varied from 4 to 8.

In Figure 4, we show the behavior of the overall integral Θ for fixed values of the core radius ($R = 20$ Å; panel A) and the shell thickness ($H = 20$ Å, panel B). From Figure 4A, we can see that the initial increase of R from 0 to R_{cl} (electron core localization radius) induces a faster drop in Θ in h/e structures compared to that in e/h structures ($\Theta_{h/e} < \Theta_{e/h}$). This behavior reflects the fact that heavier particles (holes in our case) localize more readily within a potential well (i.e., localization is produced by a “shallower” well) than lighter particles (electrons). When both particles are already localized ($R > R_{cl}$), a further increase in R then has an opposite effect. In this range of core radii, the electron–hole overlap is primarily due to penetration of the tail of a wavefunction of a shell-localized carrier into the core. Therefore, the drop in Θ in the range of $R > R_{cl}$ occurs faster in e/h structures (shell-localized holes) than in h/e structures (shell-localized electrons). The trends observed in Figure 4B (R is fixed and H is varied) can be explained by similar arguments applied to the case of a varied shell-confinement potential.

As evident from Figures 2 and 3 the strength of X–X repulsion (i.e., the X–X interaction energy) can be enhanced by providing better electron–hole spatial separation. Therefore, the e/h nanostructures that show faster initial drop of

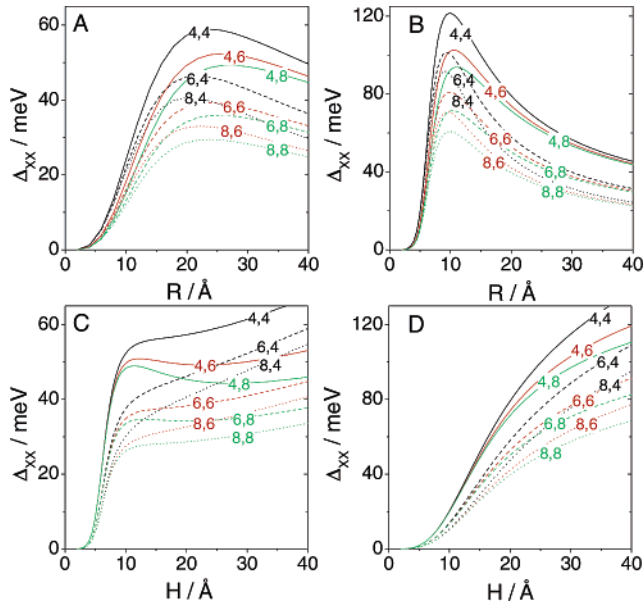


Figure 5. The X–X interaction energy Δ_{XX} plotted for different values of dielectric constants ϵ_1 (coded by line type) and ϵ_2 (coded by line color): $\epsilon_1 = 4$ (solid lines), $\epsilon_1 = 6$ (dashed lines), $\epsilon_1 = 8$ (dotted lines); $\epsilon_2 = 4$ (black), $\epsilon_2 = 6$ (red), and $\epsilon_2 = 8$ (green). Panels A and B show Δ_{XX} as a function of core radius R for a fixed shell width ($H = 20$ Å) for e/h and h/e nanostructures, respectively. Panels C and D show Δ_{XX} as a function of H for a fixed core radius ($R = 20$ Å) for e/h and h/e nanostructures, respectively.

Θ with increasing R should also show a faster initial increase in Δ_{XX} compared to the h/e structures. This trend is clearly seen in parts A and B of Figure 5. More complex trends are observed for larger core radii for which the magnitude of Δ_{XX} is determined by the interplay between the electron–hole spatial separation (increases Δ_{XX}) and the effective reduction in the density of interacting charges (decreases Δ_{XX}). This interplay produces a faster decrease in Δ_{XX} with increasing R in the case of the h/e structures compared to that in the e/h structures. Analogous considerations can be applied in the analysis of correlations between behaviors of Δ_{XX} (Figure 5C,D) and Θ (Figure 4B) for the case where R is fixed and H is varied.

In order to better understand the dependence of Δ_{XX} on the dielectric parameters of NCs, we rewrite the expression for the X–X interaction energy (eq 12) by separating the ϵ_1 - and ϵ_2 -dependent contributions

$$\Delta_{XX} = \frac{1}{\epsilon_1} \Delta_{XX}^{(1)} + \frac{1}{\epsilon_2} \Delta_{XX}^{(2)} \quad (15)$$

Assuming that the carriers are completely separated between the core and the shell, we can present $\Delta_{XX}^{(1)}$ as

$$\Delta_{XX}^{(1)} = -\frac{q_e^2}{R} + q_e^2 \int_0^R dr_1 r_1^2 \int_0^R dr_2 r_2^2 \frac{\rho^c(r_1)\rho^c(r_2)}{\max(r_1 r_2)} \quad (16)$$

where ρ^c is the electron (e/h structures) or the hole (h/e structures) density. In eq 16, the first term is a negative

(attractive) contribution from the core–shell interface polarization (U_{XX}), and the second term is a positive contribution from the repulsive Coulomb interaction between the same type of particles (two electrons or two holes) localized in the core. The $\Delta_{XX}^{(2)}$ component in eq 15 can be calculated as

$$\Delta_{XX}^{(2)} = \frac{q_e^2}{R} - q_e^2 \int_R^{R+H} dr r^2 \frac{\rho^s(r)}{r} + q_e^2 \int_R^{R+H} dr_1 r_1^2 \int_R^{R+H} dr_2 r_2^2 \frac{\rho^s(r_1)\rho^s(r_2)}{\max(r_1 r_2)} \quad (17)$$

where ρ^s is the density of shell-localized charge, which is an electron in the h/e structures and a hole in the e/h structures. Here, the first term is the contribution from the interface polarization, which has a positive sign (repulsive interaction). The second term is a negative (attractive) contribution due to direct Coulomb coupling between electrons and holes separated between the core and the shell. Finally, the third term is a positive (repulsive) energy due to the Coulomb interaction between the same sign particles that reside in the shell region.

A numerical analysis of eqs 16 and 17 indicates that both $\Delta_{XX}^{(1)}$ and $\Delta_{XX}^{(2)}$ are always positive. Therefore, the decrease in either of the dielectric constants ϵ_1 or ϵ_2 results in increasing values of Δ_{XX} . Furthermore, we find that $\Delta_{XX}^{(1)}$ is significantly greater than $\Delta_{XX}^{(2)}$ ($\Delta_{XX}^{(2)}/\Delta_{XX}^{(1)} < 0.2$). This result implies that for the structures considered here the dielectric parameter that affects the X–X interaction in the largest degree is the dielectric constant of the core as also seen in Figure 5.

Conclusions. In conclusion, we have performed analytical and numerical analysis of X–X interactions in type II core/shell NCs. These nanostructures can provide almost complete spatial separation between electron and hole wavefunctions, which leads to a significant nonzero local charge density associated with a single electron–hole (exciton) state. Under this condition, the X–X interactions can be accurately treated using first-order perturbation theory, while this approach is not appropriate in the case of type I structures, in which nearly identical spatial distributions of electron and hole wavefunctions leads to local charge quasi-neutrality.

In our modeling, we account for contributions from both the direct Coulomb coupling between charge carriers and the interface polarization. Both of these contributions vary in correlation with the electron–hole overlap integral Θ , and specifically, they increase as Θ decreases. This result indicates enhancement in the X–X Coulomb interaction with increasing degree of spatial separation between electrons and holes. We observe that direct Coulomb coupling in the case of charge-separated states always leads to strong X–X repulsion.

On the other hand, the contribution from interface polarization can be either repulsive or attractive depending on the relationship between the core and the shell dielectric constants. However, the latter only provides a relatively small ($\approx 30\%$) correction to the total X–X interaction energy.

Therefore, the sign of Δ_{XX} is always positive indicating overall X–X repulsion. Further, our calculations show that the X–X interaction in these structures can be characterized by giant energies on the order of 100 meV. These values are comparable to or greater than typical transition line widths in NC samples, indicating the feasibility of the situation for which the Coulomb shift of optical transitions in singly excited NCs almost completely suppresses absorption at the emission wavelength. Under these conditions optical amplification in NCs can be achieved in the single-exciton regime, which should allow one to eliminate the complication associated with ultrafast optical gain decay induced by multiparticle Auger recombination.

Acknowledgment. This work was supported by the Chemical Sciences, Biosciences, and Geosciences Division of the Office of Basic Energy Sciences, Office of Science, U.S. Department of Energy and Los Alamos LDRD funds. S.A.I, S.T., and V.I.K. acknowledge support by the Center for Integrated Nanotechnologies (CINT), a U.S. Department of Energy, Office of Basic Energy Sciences nanoscale science research center operated jointly by Los Alamos and Sandia National Laboratories. A.P. acknowledges support by the Center for Nonlinear Studies (CNLS).

References

- (1) Hines, M. A.; Guyot-Sionnest, P. *J. Phys. Chem.* **1996**, *100*, 468.
- (2) Dabbousi, B. O.; RodriguezViejo, J.; Mikulec, F. V.; Heine, J. R.; Mattoussi, H.; Ober, R.; Jensen, K. F.; Bawendi, M. G. *J. Phys. Chem. B* **1997**, *101*, 9463.
- (3) Peng, X. G.; Schlamp, M. C.; Kadavanich, A. V.; Alivisatos, A. P. *J. Am. Chem. Soc.* **1997**, *119*, 7019.
- (4) Cao, Y. W.; Banin, U. *Angew. Chem., Int. Ed. Engl.* **1999**, *38*, 3692.
- (5) Micic, O. I.; Smith, B. B.; Nozik, A. J. *J. Phys. Chem. B* **2000**, *104*, 12149.
- (6) Talapin, D. V.; Mekis, I.; Gotzinger, S.; Kornowski, A.; Benson, O.; Weller, H. *J. Phys. Chem. B* **2004**, *108*, 18826.
- (7) Donega, C. D.; Liljeroth, P.; Vanmaekelbergh, D. *Small* **2005**, *1*, 1152.
- (8) Kim, S.; Fisher, B.; Eisler, H. J.; Bawendi, M. *J. Am. Chem. Soc.* **2003**, *125*, 11466.
- (9) Balet, L. P.; Ivanov, S. A.; Piryatinski, A.; Achermann, M.; Klimov, V. I. *Nano Lett.* **2004**, *4*, 1485.
- (10) Ivanov, S. A.; Nanda, J.; Piryatinski, A.; Achermann, M.; Balet, L. P.; Bezel, I. V.; Anikeeva, P. O.; Tretiak, S.; Klimov, V. I. *J. Phys. Chem. B* **2004**, *108*, 10625.
- (11) Yu, K.; Zaman, B.; Romanova, S.; Wang, D. S.; Ripmeester, J. A. *Small* **2005**, *1*, 332.
- (12) Klimov, V. I.; Mikhailovsky, A. A.; Xu, S.; Malko, A.; Hollingsworth, J. A.; Leatherdale, C. A.; Eisler, H. J.; Bawendi, M. G. *Science* **2000**, *290*, 314.
- (13) Kraebel, B.; Malko, A.; Hollingsworth, J.; Klimov, V. I. *Appl. Phys. Lett.* **2001**, *78*, 1814.
- (14) Petruska, M. A.; Malko, A. V.; Voyles, P. M.; Klimov, V. I. *Adv. Mater.* **2003**, *15*, 610.
- (15) Schaller, R. D.; Klimov, V. I. *Phys. Rev. Lett.* **2004**, *92*, 186601.
- (16) Schaller, R. D.; Agranovich, V. M.; Klimov, V. I. *Nat. Phys.* **2005**, *1*, 189.
- (17) Klimov, V. I.; Mikhailovsky, A. A.; McBranch, D. W.; Leatherdale, C. A.; Bawendi, M. G. *Science* **2000**, *287*, 1011.
- (18) Nanda, J.; Ivanov, S. A.; Htoon, H.; Bezel, I.; Piryatinski, A.; Tretiak, S.; Klimov, V. I. *J. Appl. Phys.* **2006**, *99*, 034309.
- (19) Achermann, M.; Hollingsworth, J. A.; Klimov, V. I. *Phys. Rev. B* **2003**, *68*, 245302.
- (20) Butov, L. V.; Gossard, A. C.; Chemla, D. S. *Nature* **2002**, *418*, 751.
- (21) Banyai, L.; Hu, Y. Z.; Lindberg, M.; Koch, S. W. *Phys. Rev. B* **1988**, *38*, 8142.
- (22) Banyai, L. *Phys. Rev. B* **1989**, *39*, 8022.
- (23) Takagahara, T. *Phys. Rev. B* **1989**, *39*, 10206.
- (24) Hu, Y. Z.; Lindberg, M.; Koch, S. W. *Phys. Rev. B* **1990**, *42*, 1713.
- (25) Efros, Al. L.; Rodina, A. V. *Solid State Commun.* **1989**, *72*, 645.
- (26) Grigoryan, G. B.; Rodina, A. V.; Efros, Al. L. *Sov. Phys. Solid State* **1990**, *32*, 2037.
- (27) Efros, A. L.; Rosen, M. *Annu. Rev. Mater. Sci.* **2000**, *30*, 475.
- (28) Haus, J. W.; Zhou, H. S.; Honma, I.; Komiyama, H. *Phys. Rev. B* **1993**, *47*, 1359.
- (29) Jackson, J. D. *Classical Electrodynamics*: John Wiley: New York, 1975.
- (30) Higher order roots I_n^a and q_n^a ($n = 2, 3, 4, \dots$) correspond to higher-energy nS states. Corresponding wavefunctions have the same form as those in eq 1. Our calculations can be extended to these nS states by simply replacing the $1S$ wavefunction with the nS wavefunctions.

NL0622404